nature neuroscience

Mural lymphatic endothelial cells regulate meningeal angiogenesis in the zebrafish

Neil I Bower[1], Katarzyna Koltowska[1], Cathy Pichol-Thievend[1], Isaac Virshup[2], Scott Paterson[1], Anne K Lagendijk[1], Weili Wang[1], Benjamin W Lindsey[3], Stephen J Bent[1], Sungmin Baek[1], Maria Rondon-Galeano[1], Daniel G Hurley[2], Naoki Mochizuki[4,5], Cas Simons[1], Mathias Francois[1], Christine A Wells[2], Jan Kaslin[3] & Benjamin M Hogan[1]

Mural cells of the vertebrate brain maintain vascular integrity and function, play roles in stroke and are involved in maintenance of neural stem cells. However, the origins, diversity and roles of mural cells remain to be fully understood. Using transgenic zebrafish, we identified a population of isolated mural lymphatic endothelial cells surrounding meningeal blood vessels. These meningeal mural lymphatic endothelial cells (muLECs) express lymphatic endothelial cell markers and form by sprouting from blood vessels. In larvae, muLECs develop from a lymphatic endothelial loop in the midbrain into a dispersed, nonlumenized mural lineage. muLEC development requires normal signaling through the Vegfc–Vegfd–Ccbe1–Vegfr3 pathway. Mature muLECs produce vascular growth factors and accumulate low-density lipoproteins from the bloodstream. We find that muLECs are essential for normal meningeal vascularization. Together, these data identify an unexpected lymphatic lineage and developmental mechanism necessary for establishing normal meningeal blood vasculature.

The blood vessels of the CNS are regulated by the neurovascular unit and are contiguous with meningeal blood vessels, which extend between the pia mater and arachnoid in mammals. Neurovascular vessels are comprised of endothelial cells (ECs), mural and intramural cells, which occur in close proximity to one another and are functionally interdependent, forming the mature blood brain barrier (BBB)[1]. The neurovasculature is essential for tissue homeostasis, supplying the brain with oxygen, essential nutrients and immune cells; defects are associated with cognitive deficits and neurodegenerative disorders[1–3]. Known mural lineages that include smooth muscle, macrophages and microglia, as well as intramural pericytes, have been variously implicated in vascular permeability, vascular integrity, neurovascular coupling and the maintenance of neural stem cells[1,3]. Pericytes play an important role in regulating formation of the BBB, and CNS capillaries have a greater level of pericyte coverage than those of other tissues, indicative of their tight control over neurovascular function[1,3]. Macrophages and microglia are essential for clearance of debris and pathogens surrounding vessels[4]. Furthermore, the endfeet of astrocytes cover large areas of blood vessels and have been implicated in regulation of the endothelial metabolic barrier[1,5]. Despite these many important cell lineages and functions, much remains to be uncovered about how these cells interact with each other, as well as local differences in mural cell functions between the CNS and meninges.

The lymphatic vasculature is a network of blind-ended vessels distributed throughout most of the body. Lymphatic vessels control tissue fluid homeostasis by removing excess fluid from the interstitium and also regulate the peripheral immune response, primarily by acting as a route for the trafficking of lymphocytes[6]. Despite the important functions of lymphatics in most tissues, the CNS is immune-privileged and was long considered devoid of lymphatic vessels. While the presence of putative meningeal lymphatic vessels had been noted previously[7,8], it was recently established that meningeal lymphatics present on the dura mater can in fact function to drain cerebrospinal fluid (CSF) and lymphocytes from the CNS[9,10]. The discovery that an outer meningeal lymphatic vasculature plays a role in CNS homeostasis may suggest that it plays a modulatory role in neuroinflammatory or neurodegenerative disorders. Nevertheless, these vessels are dural and no lymphatic endothelial cells have been described in the CNS during either development or homeostasis.

Angiogenesis, the sprouting of new blood vessels from existing vessels, is regulated by proangiogenic growth factors such as Vegfa (refs. 11,12). These growth factors can be released from ECs, stromal cells and leukocytes; they promote vessel sprouting and provide guidance cues for developing vessels[11]. Abnormal angiogenesis in the CNS can contribute to the development of pathological conditions, including neurodegenerative diseases and arteriovenous malformations, and angiogenesis is required for recovery from ischemic stroke and brain injury[13–15]. Lymphangiogenesis, the formation of the lymphatic vasculature from pre-existing vessels, occurs when lymphatic endothelial cells (LECs) sprout from veins. In the zebrafish trunk and face,

[1]Division of Genomics of Development and Disease, Institute for Molecular Bioscience, The University of Queensland, St Lucia, Brisbane, Australia. [2]Centre for Stem Cell Systems, Department of Anatomy and Neuroscience, Faculty of Medicine Dentistry and Health Sciences, The University of Melbourne, Victoria, Australia. [3]Australian Regenerative Medicine Institute, Monash University Clayton Campus, Clayton, Victoria, Australia. [4]Department of Cell Biology, National Cerebral and Cardiovascular Center Research Institute, Suita, Osaka, Japan. [5]AMED-CREST, National Cerebral and Cardiovascular Center, Suita, Osaka, Japan. Correspondence should be addressed to B.H. (b.hogan@imb.uq.edu.au).

Received 11 March; accepted 31 March; published online 1 May 2017; doi:10.1038/nn.4558

lymphangiogenesis is dependent on the Ccbe1–Vegfc–Vegfr3 (formally Flt4) signaling axis, with mutants lacking a lymphatic vasculature[16–18]. In addition to the apical role of the ligand Vegfc, Vegfd acts in a partially redundant manner during the formation of some lymphatic vessels in zebrafish[19,20]. To date, the formation and function of lymphatics in or around the zebrafish brain remain to be described.

In this study, while examining zebrafish meningeal lymphatics, we identified a previously uncharacterized population of mural LECs that were present at the meningeal blood vasculature. These cells express molecular markers of lymphatics and are a distinct population from ECs, pericytes, macrophages or astrocytes. During development, they sprout from existing blood vessels in the CNS in a *vegfc*-, *vegfd*-, *ccbe1*- and *vegfr3*-dependent manner. muLECs contain large inclusions similar in appearance to lipid-laden or fluorescent granular perithelial cells in mammals[21,22] and actively take up low-density lipoproteins (LDL) from the blood vasculature. Furthermore, muLECs express proangiogenic growth factors and are essential for normal meningeal vascularization. The identification of this cell type, with its unexpected developmental origins, furthers our understanding of the functional components of the neurovasculature in vertebrates.

RESULTS

Identification of meningeal mural LECs at adult and larval stages

To determine whether meningeal lymphatics were present in zebrafish, we examined the presence and morphology of vasculature in adult zebrafish brains using the double-transgenic *Tg(-5.2lyve1b:DsRed)^{nz101};Tg(kdrl:EGFP)^{s843}* strain. The *lyve1b* (hereafter *lyve1*) promoter drives expression in lymphatics and the *kdrl* promoter drives expression in blood vessels in zebrafish[23,24]. We were unable to identify meningeal lymphatics after dissecting out adult brains but observed *lyve1*-expressing, *kdrl*-negative vessels that remained attached to the skull during dissection, consistent with findings in mice[10]. During this examination, we unexpectedly identified a *lyve1*-expressing cell population associated with blood vessels at the surface of the brain (**Fig. 1a–j**). At single-cell resolution, we noted that these cells appeared to contain large vacuoles or inclusions (**Fig. 1c**). By analyzing co-localization with *lyve1* expression in double-transgenic animals, we found that these cells also expressed from the *prox1a* promoter, detected in our transgenic fish using *Tg(prox1a:KalTA4^{uq3bh};10xUAS:Venus)*, and from the *fli1a* promoter, detected using *Tg(fli1a:nEGFP^{y7})*, indicating they were likely LECs (**Supplementary Fig. 1a,b**). *lyve1* co-expression with transgenic *prox1a* was mosaic, as expected because the *prox1a* transgenic line utilizes *KaltA4* and *10xUAS*, which provide bright but mosaic expression due to silencing of the repetitive UAS element[25]. Sectioning revealed that the cells were restricted around peripheral blood vessels at the meninx (homologous to mammalian meninges) and were not present in the deeper tissues (**Fig. 1e–j**). This muLEC population was found in the forebrain, midbrain and hindbrain (**Fig. 1i**), and it was also present around major arteries entering the brain ventrally (**Fig. 1j**). Quantification confirmed that muLECs were significantly enriched at the meninx ($P < 0.0001$; **Supplementary Fig. 1c,d**) and displayed a density of 3.6 cells per 100 µM along vessels at the adult meningeal blood vasculature. muLECs did not form lumenized vessels (**Fig. 1b,c**) and were not observed in other organs examined (heart, kidney, liver, spleen, gastrointestinal tract; data not shown).

We next examined vessels in the zebrafish brain during larval stages when the skull did not need to be removed in order to directly image the neurovasculature. We identified lymphatic vessels expressing both *lyve1* and *prox1a* in 7-mm *Tg(prox1a:KalTA4^{uq3bh};10xUAS:Venus)* larvae (**Fig. 2a,b**). The vessels extended

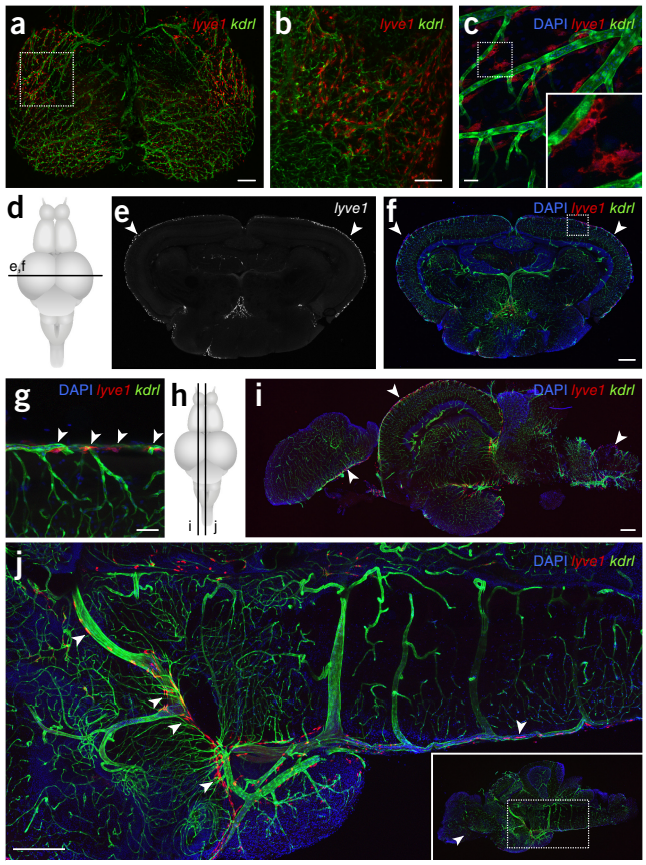

Figure 1 Mural lymphatic endothelial cells are present at the adult meninx. (**a**) Dorsal confocal image of a 12-month-old adult *Tg(-5.2lyve1b:DsRed)^{nz101};Tg(kdrl:EGFP)^{s843}* zebrafish diencephalon, showing the presence of *lyve1*-expressing cells (red) adjacent to *kdrl-EGFP*-expressing blood vessels (green). Representative image of $n = 6$ adult male and female brains analyzed. Scale bar, 200 µm. (**b**) Higher magnification of dashed outline in **a**, showing *lyve1*-expressing cells adjacent to *kdrl-EGFP*-expressing blood vessels. Scale bar, 100 µm. (**c**) Higher magnification of region equivalent to **b** (inset: boxed region), showing that *lyve1*-expressing cells do not form lumenized vessels and appear to contain vacuoles. Scale bar, 25 µm. (**d–f**) Confocal images of a cross-section, indicated by the horizontal bar in **d**, of a 12-month-old adult zebrafish diencephalon showing *lyve1*-expressing cells present in the meninx (arrowheads). Representative images of $n = 3$ sectioned male and female adult brains analyzed. Scale bar, 200 µm. (**g**) Magnification of boxed region in **f** showing *lyve1*-expressing cells (arrowheads) present only adjacent to blood vessels in the meninx. Representative image of $n = 3$ sectioned adult brains analyzed. Scale bar, 20 µm. (**h**) Schematic diagram showing the sagittal sections (vertical lines) in **i** and **j**. (**i**) Confocal image of a sagittal section of a 12-month-old adult zebrafish brain showing *lyve1*-expressing cells (muLECs) present in the forebrain, midbrain and hindbrain (arrowheads). Representative image of $n = 3$ sectioned male and female adult brains analyzed; scale bar represents 200 µm. (**j**) Magnification of region shown in the inset, showing confocal image of a sagittal section of muLECs adjacent to the major arteries entering the brain ventrally in an adult zebrafish brain (arrowheads). Scale bar, 200 µm.

from the otolithic lymphatic vessel, along the midbrain–hindbrain boundary and over the dorsal region of the larval hindbrain (**Fig. 2a,b**). These cells surrounded the outer curvature of the brain, suggesting the presence of meningeal lymphatics (**Fig. 2c** and **Supplementary Movie 1**). At the same stage, we identified a separate population of cells co-expressing *lyve1* and *prox1a* over the midbrain

that did not form lumenized vessels (**Fig. 2a**,**b** and **Supplementary Fig. 1e**), similarly to the cells observed in adults. The larval meningeal lymphatics took up high-molecular-weight (MW) dextran following intracranial injection, whereas the dispersed cells did not display this capability (**Supplementary Fig. 2a**,**b**). To confirm that these cells were endothelial, we examined double transgenic embryos and confirmed co-expression of *fli1a* together with *lyve1* (**Supplementary Figs. 1f** and **2c**,**d**).

In larvae, muLECs associated more closely with blood vessels than the parenchyma and resided closer to branch points than midpoints of vessels (**Supplementary Fig. 1g**,**h**). Their close proximity with blood vessels may have been consistent with them having a pericyte identity. The best current available marker for pericytes in zebrafish is expressed from *pdgfrβ*, which labels pericytes and neural crest derived cells in the brain[26]. We generated a pericyte reporter transgenic line, *TgBAC(pdgfrβ:EGFP)*^{uq15bh}, using a previously described bacterial artificial chromosome (BAC) construct[26], and found that the muLECs were a distinct population from *pdgfrβ*-expressing pericytes along blood vessels (**Fig. 2d**–**f**). muLECs localized in a distinctive and more distal position relative to the vessel wall than the *pdgfrβ*-expressing pericytes (**Fig. 2d**–**f**). In adults, pericytes were present throughout the entire brain vasculature (**Supplementary Fig. 2f**), but muLECs were exclusively meningeal (**Fig. 1e**,**f** and **Supplementary Fig. 1c**,**d**). The muLECs did not display any morphological similarities (location, morphology) with previously described zebrafish microglial or macrophage populations[27], and examination of expression from the validated macrophage promoter *mpeg1*, detected with a *Tg(mpeg1:mcherry)* construct[28], confirmed that there was no co-localization with *prox1a* (**Fig. 2g** and **Supplementary Fig. 1e**). Additionally, markers of smooth muscle (encoded by *TgBAC(acta2:EGFP)*^{uq17bh}) and neuronal and/or oligodendrocyte (encoded by *Tg(nkx2.2a:EGFP)*^{vu16Tg}) populations were not co-expressed with *lyve1* in muLECs (**Supplementary Figs. 1f** and **3a**–**d**). Hence, muLECs were anatomically distinct from pericytes, macrophages, smooth muscle, blood vessel ECs and *nkx2.2*-expressing neurons or oligodendrocytes.

muLECs develop from a lymphatic endothelial loop that originates from embryonic blood vessels

To identify the origin of muLECs, we examined the cranial vasculature in larvae 5 d postfertilization (dpf). We noticed the presence of a lymphatic endothelial loop, labeled by strong *lyve1-DsRed* expression in the midbrain (**Fig. 3a** and **Supplementary Fig. 4**). At 5dpf, the *lyve1-DsRed*-expressing cells co-expressed *prox1a* and *fli1a* (**Supplementary Fig. 4b**,**c**), and angiography using low-MW dextran demonstrated that they did not contain blood (**Supplementary Fig. 4d**). By imaging this cell population over time, from 5 dpf to 15 dpf, we observed that the cells of the lymphatic loop gradually appeared more mesenchymal in morphology (**Fig. 3a**–**c**). In larvae, the *lyve1*-expressing vascular-loop-derived cells progressively covered the midbrain and became closely associated with blood vessels (**Fig. 3d**). Using a lineage tracing approach that took advantage of Kaede photoconversion, we generated a *Tg(prox1a:KalTA4)*^{uq3bh}*;Tg(10xUAS:Kaede)*^{s1999t} strain and then photoconverted this cell population at 5 dpf, before analyzing at 10 dpf (**Fig. 3e**). This approach confirmed that the cells that made up the lymphatic loop individually became more mesenchymal (**Fig. 3f**,**g** and **Supplementary Fig. 5a**,**b**). Progressive, serial photoconversions from 10–20 dpf with analysis every 5 d after conversion confirmed that these cells were not replaced with an independent population over time and actively expanded in number (**Fig. 3g** and **Supplementary Fig. 5c**).

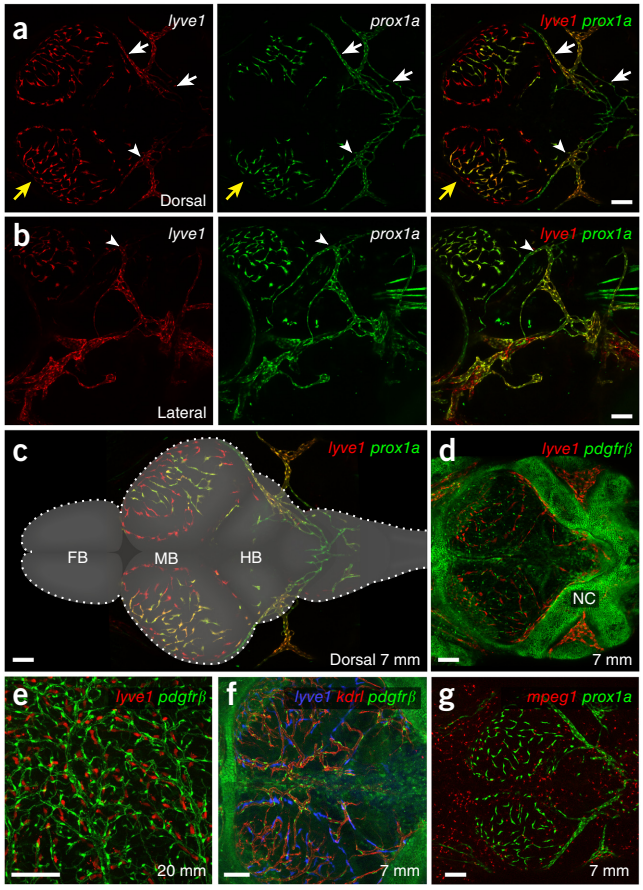

Figure 2 muLECs and meningeal lymphatics are present in the zebrafish larval brain. (**a**) Dorsal and (**b**) lateral confocal images of 7-mm *Tg(-5.2lyve1b:DsRed)*^{nz101}*;Tg(prox1a:KalTA4*^{uq3bh}*;10xUAS:Venus)* midbrain and hindbrain. White arrows indicate the presence of lymphatic vessels co-expressing *prox1a* and *lyve1* at the level of the brain connected to the otolithic lymphatic vessel (arrowheads; $n = 6$ larvae). muLECs are indicated by a yellow arrow. Expression of *prox1a* is mosaic due to use of the KaltA4–UAS system[25]. See **Supplementary Figure 1e** for quantification. Scale bars, 100 µm. (**c**) Dorsal confocal image of 7-mm embryo with a schematic overlay of the brain showing the location of cells co-expressing *prox1a* and *lyve1*. FB, forebrain; MB, midbrain; HB, hindbrain; scale bar, 100 µm. (**d**) Dorsal confocal image of *Tg(-5.2lyve1b:DsRed)*^{nz101}*;Tg(pdgfrβ:EGFP)*^{uq15bh} 7-mm larvae showing *lyve1*-expressing muLECs forming a distinct population to the *pdgfrβ*-expressing pericytes (196 cells from $n = 3$ larvae). NC, neural-crest-derived cells; scale bar, 100 µm. (**e**) Confocal image of the surface of the brain, showing muLECs present in a more distal mural niche than perivascular pericytes ($n = 2$ adult brains). Scale bar, 100 µm. (**f**) Dorsal confocal image of *Tg(-5.2lyve1b:BFPCaax)*^{uq18bh}*;Tg(pdgfrβ:EGFP)*^{uq15bh}*;Tg(kdrl:Cherry)*^{s916} showing the three distinct cell types: muLECs (blue), pericytes (green) and endothelial cells (red; 172 cells from $n = 2$ larvae). Scale bar, 100 µm. (**g**) Dorsal confocal image of *Tg(mpeg1:mcherry);Tg(prox1a:KalTA4*^{uq3bh}*;10xUAS:Venus)* 7-mm larvae[28] showing *prox1a*-expressing muLECs forming a population distinct from *mpeg1*-expressing macrophages ($n = 11$ larvae; scale bar, 100 µm). See **Supplementary Figure 1f** for quantification.

To determine the earlier developmental origin of the lymphatic loop in the midbrain, we performed time lapse imaging of *Tg(-5.2lyve1b:DsRed)*^{nz101}*;Tg(fli1a:nEGFP)*^{y7} cells from 30 h postfertilization (hpf) to 4 dpf (**Fig. 3h**–**k**, **Supplementary Movie 2** and **Supplementary Fig. 6**). This double transgenic line allows the tracing of individual EC nuclei as they move through the embryo and, with single-cell resolution, allows analysis of *lyve1* expression. At approximately

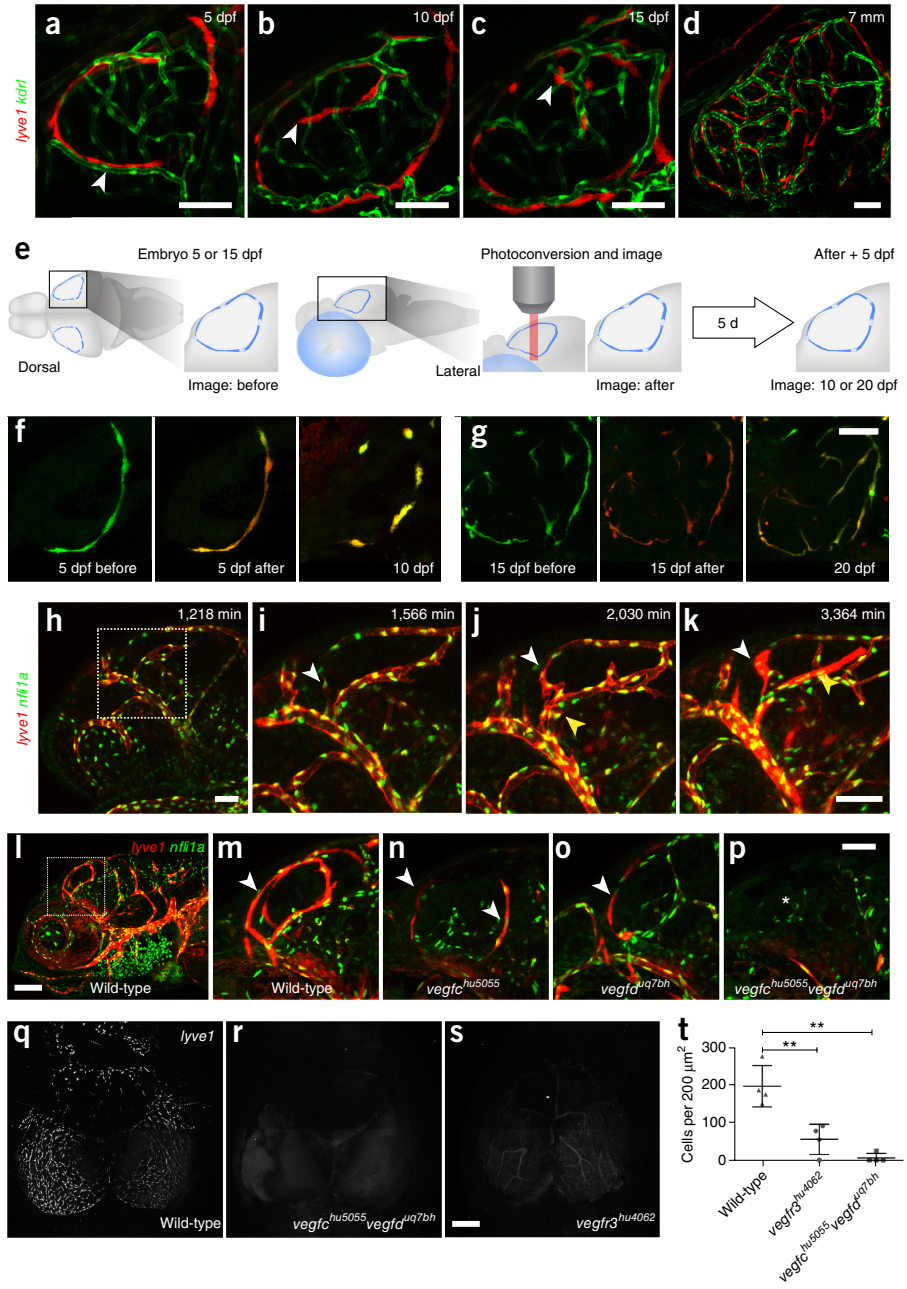

Figure 3 muLECs form by sprouting lymphangiogenesis and disperse throughout the larval meninx. (**a**–**c**) Dorsal confocal images of cells over the right side of the midbrain in *Tg(-5.2lyve1b:DsRed)*^{nz101}*;Tg(kdrl:EGFP)*^{s843} from 5 to 15 dpf showing *lyve1*-expressing cells of the vascular loop becoming progressively mesenchymal in appearance (arrowheads; $n = 5$ larvae per timepoint; scale bar, 50 µm). (**d**) *lyve1*-expressing cells are adjacent to *kdrl-expressing* blood vessels in 7-mm embryos ($n = 6$ larvae; scale bar, 50 µm). (**e**) Schematic diagram showing experimental design for Kaede experiments. (**f**,**g**) Confocal images of *Tg(prox1a:KalTA4)*^{uq3bh}*;Tg(10xUAS:Kaede)*^{s1999t} (**f**) before (left) and after (middle) photoconversion at 5 dpf and (right) reimaged at 10 dpf; or (**g**) before (left) and after (middle) photoconversion at 15 dpf and (right) reimaged at 20 dpf (**Supplementary Fig. 3**). Positive lineage-tracing over a serial 5-d period revealed that a single cell population expanded (5–10 dpf, $n = 18$ cells counted from 3 embryos; 15–20 dpf, $n = 53$ cells from 6 embryos). Additional data and quantification of cell expansion are provided in **Supplementary Figure 5a**–**c**. Scale bar, 50 µm. (**h**–**k**) Time-lapse imaging (lateral view) from 30 hpf to 94 hpf shows cells that give rise to the lymphatic vascular loop, sprout from the choroidal vascular plexus that develops parallel to the primary head sinus (arrowheads). The timestamp corresponds to time elapsed since 30 hpf (**Supplementary Movie 2**); $n = 4$ independent movies confirmed this cellular origin. Scale bar, 50 µm; **i**–**k** show magnified view of the region outlined in **h**. (**l**) Lateral confocal images of a wild-type 5-dpf *Tg(-5.2lyve1b:DsRed)*^{nz101}*;Tg(fli1a:nEGFP)*^{y7} zebrafish embryo showing the putative lymphatic loop. Representative image of $n = 7$ embryos analyzed. Scale bar, 100 µm. (**m**–**p**) Confocal images of the boxed area in **l**, showing that the loop that forms in (**m**) wild-type embryos (arrowhead; $n = 7$ embryos) is reduced in (**n**) *vegfc*^{hu5055} (arrowheads; $n = 6$ embryos) and (**o**) *vegfd*^{uq7bh} (arrowhead; $n = 6$ embryos) single mutants but is absent in (**p**) *vegfc*^{hu5055}*vegfd*^{uq7bh} double mutants (asterisk; $n = 9$ embryos). Additional data and quantification of cell numbers are shown in **Supplementary Figure 7a**–**i**. Scale bar, 50 µm. (**q**–**s**) Dorsal confocal images showing the muLECs present in 3-month-old (**q**) wild-type adult fish ($n = 4$ adult brains) are absent in (**r**) *vegfc*^{hu5055}*vegfd*^{uq7bh} double mutants ($n = 4$ adult brains) and (**s**) *vegfr3*^{hu4062} mutants ($n = 4$ adult brains). Scale bar, 200 µm. (**t**) Quantification of *lyve1*-expressing cells in 500 µm^2 in 3-month-old male and female wild-type ($n = 4$ adult brains), *vegfr3*^{hu4062} single-mutant ($n = 4$ adult brains) and *vegfc*^{hu5055}*vegfd*^{uq7bh} double-mutant ($n = 4$ adult brains) fish. Error bars represent mean ± s.e.m.; $^{**}P < 0.01$, from one way ANOVA ($F_{2,10} = 14.69$).

54 hpf, ECs migrated dorsally from the choroidal vascular plexus in the developing CNS and were observed to progressively upregulate *lyve1-DsRed* as they migrated peripherally; they gave rise to the lymphatic loop by 4 dpf. Hence, this newly identified population of muLECs formed by initial sprouting lymphangiogenesis from local veins in the CNS, followed by a change to a more mesenchymal morphology (5–15 dpf) as the population expanded.

muLEC sprouting is dependent upon Vegfc, Vegfd, Ccbe1 and Vegfr3 signaling

As lymphangiogenic sprouting requires Vegfc (and/or Vegfd), Ccbe1 and Vegfr3 signaling[29], we analyzed muLEC development in *vegfc*^{hu5055} and *vegfd*^{uq7bh} mutants[20]. We found that in larvae, the cells populating the lymphatic loop were vastly reduced in individual *vegfd*^{uq7bh} and *vegfc*^{hu5055} mutants and completely absent in *vegfc*^{hu5055}*vegfd*^{uq7bh} double mutants (**Fig. 3l–p** and **Supplementary Fig. 7a–i**). The formation of the lymphatic loop at 5 dpf was also blocked upon injection of morpholinos targeting *vegfr3* or *ccbe1*[16] (**Supplementary Fig. 7j–m**). Next, we analyzed adult *Tg(-5.2lyve1b:DsRed)*^{nz101}, *vegfr3*^{hu4062} single-mutant and *vegfc*^{hu5055}*vegfd*^{uq7bh} double-mutant fish, which are hypomorphic and viable as adults. In both *vegfr3*^{hu4062} mutants and in *vegfc*^{hu5055}*vegfd*^{uq7bh} double mutants, *lyve1*-expressing muLECs were vastly reduced or absent compared with controls (**Fig. 3q–t**). Notably, we observed *lyve1*-expressing muLECs in *vegfc*^{hu5055} and *vegfd*^{uq7bh} single-mutant fish (**Supplementary Fig. 7n,o**), demonstrating that either ligand alone was sufficient for the recovery and expansion of this population of cells by adult stages. Together, these data provide further evidence that the cells of the putative lymphatic loop give rise to muLECs in adults and demonstrate an essential role for Vegfc, Vegfd, Ccbe1 and Vegfr3 signaling in their development.

Mature muLECs display a distinctive ultrastructure and take up LDL

To better determine the location of muLECs relative to the blood vasculature and meninx, we performed immunoelectron microscopy using the *Tg(-5.2lyve1b:venus)*^{uq16} strain (**Fig. 4a,b** and **Supplementary Fig. 8a–e**). muLECs were identified adjacent to blood vessels and contained characteristic intracellular inclusions (**Fig. 1c**). muLECs were in close proximity to but not embedded in the basement membrane of ECs. The meninx was visible adjacent to the muLEC cells. These observations confirmed that muLECs were large mural cells with distinctive vacuole or inclusion body structures, closely associated with blood vessels. These features are shared with previously described lipid-laden[30] or fluorescent granular perithelial cells[21] in mammals, which take up lipids and LDL from meningeal blood vessels[22]. To test whether muLECs can take up LDL, we injected Alexa Fluor-488-labeled acetylated LDL into the posterior cardinal vein of 7-mm *Tg(-5.2lyve1b:DsRed)*^{nz101} zebrafish larvae. We examined the presence of LDL in muLECs at 3 and 24 h after injection and observed that LDL was present intracellularly in muLECs at both stages (**Fig. 4c,d**). This uptake seemed to be specific to LDL and we did not observe equivalent muLEC dye uptake upon injection with high-MW dextran (**Supplementary Fig. 8f,g**). We also performed high-MW dextran injections into the blood stream of wild-type controls and *vegfc*^{hu5055}*vegfd*^{uq7bh} double-mutant larvae, which lack muLECs. Three hours after injection, we examined the meningeal blood vasculature for leakage by confocal microscopy but did not observe dye outside of the blood vessels (**Supplementary Fig. 8h,i**). Hence, muLECs did not appear to be necessary for maintenance of vessel integrity.

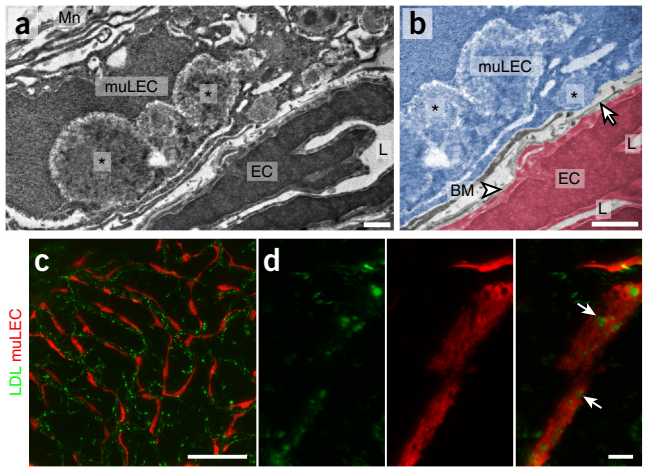

Figure 4 muLECs are immediately adjacent to endothelium and take up LDL. (**a**) Immunoelectron microscopy showing a muLEC in relation to the basement membrane (BM) of an endothelial cell and the zebrafish meninx. Large vacuoles or inclusions (asterisks) are present in the muLEC immediately adjacent to the vascular matrix. EC, endothelial cell; L, blood vessel lumen; Mn, meninx. Scale bar, 1 µm. (**b**) False-colored immunoelectron microscopy from **a**. The muLEC is proximal to but not embedded in the BM. Scale bar, 1 µm; arrowhead, BM; arrow, collagen fibers of the vascular matrix. (**c**) Dorsal confocal images of muLECs over the right side of the midbrain in *Tg(-5.2lyve1b:DsRed)*^{nz101} 3 h after Alexa Fluor-488-labeled acetylated LDL was injected into the blood stream. LDL is present in the endothelial cells as well as 61% ± 11% (mean ± s.d.) of the muLECs (n = 72 muLECs scored from 3 embryos). Scale bar, 100 µm. (**d**) 24 h after LDL injection as described above, LDL accumulated intracellularly in 100% of muLECs. Arrows, inclusions containing labeled LDL; n = 73 muLEC cells from 3 embryos. Left, LDL; middle, muLECs; right, merged image. Scale bar, 10 µm.

muLECs express LEC markers and produce vascular endothelial growth factors

To further investigate the molecular identity of adult muLECs, we separated muLECs from 12-month-old male and female adult brains by fluorescence-activated cell (FAC) sorting (**Supplementary Fig. 9a**) and performed transcriptomic profiling by RNA-seq analysis in triplicate. The sorted cells did not include the meningeal lymphatics, which remained attached to the skull following dissections. FACS analysis using *Tg(-5.2lyve1b:DsRed)*^{nz101} and *Tg(kdrl:EGFP)*^{s834}*;Tg(pdgfrβ:EGFP)*^{uq15bh} demonstrated efficient isolation of muLECs from pericytes and endothelial cells (**Supplementary Fig. 9b,c**). As further evidence of cell purity after FACS, the muLECs did not express the EC marker *kdrl,* macrophage marker *csf1r*, or the pericyte marker *pdgfrβ* in the dataset used below (**Fig. 5**).

To compare these RNA-seq data, a set of three control zebrafish RNA-seq samples were chosen as control postembryonic zebrafish tissues; adult head (Gene Expression Omnibus (GEO) accession code: GSM977959), adult tail (GEO: GSM977960) and 5-d larva (GEO: GSM977958). Comparison of global mRNA profiles with these postembryonic zebrafish tissues revealed that muLEC-enriched genes had gene ontology terms ($P < 0.05$) associated with vascular development, angiogenesis and blood vessel morphogenesis (**Fig. 5a**). Independently, we also performed RNA-seq on FAC-sorted GFP$^+$ pericytes from *Tg(pdgfrβ:EGFP)*^{uq15bh}*;Tg(kdrl:Cherry)*^{s916} adult zebrafish brains (**Supplementary Fig. 9d**) and performed unbiased comparisons of these transcriptomes with our muLEC data, our own published FAC-sorted EC dataset from 2 dpf embryos[31] and a publicly available macrophage and endothelial dataset[32]. Principle component analysis on batch-corrected data[33] globally comparing all of these

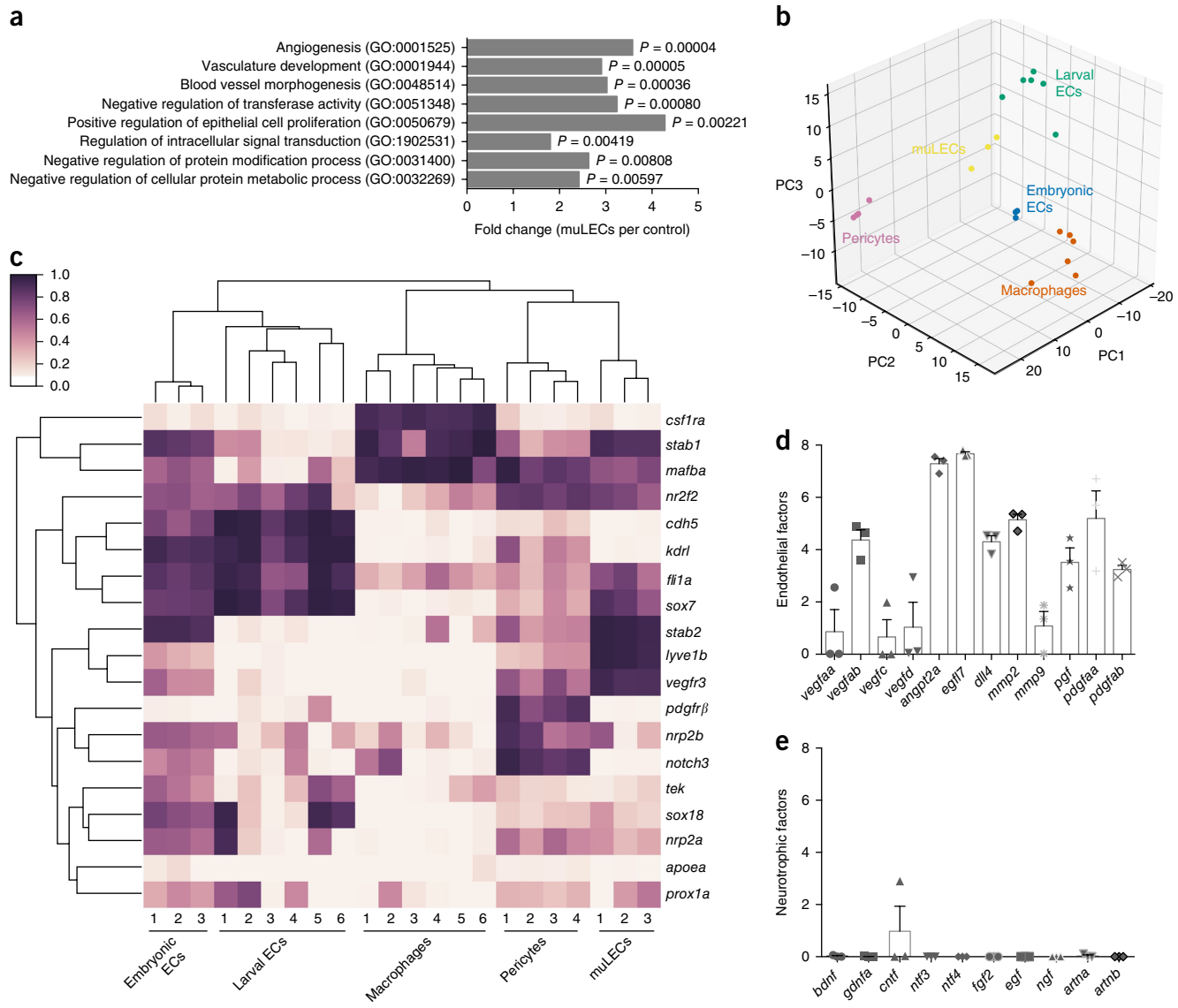

Figure 5 Mural lymphatic endothelial cells are transcriptionally distinct from other mural cell types and produce endothelial growth factors. (**a**) Gene ontology analysis of positively regulated pathways for genes differentially expressed between FAC-sorted muLECs ($n = 3$ FAC sorts) and 3 independent postembryonic zebrafish tissues (adult head, adult tail and 5-d larvae). *P* values represent Bonferroni-adjusted values. Gene ontology codes: 0001525, 0001944, 0048514, 0051348, 0050679, 1902531, 0031400 and 0032269. (**b**) Three-dimensional principle component (PC) analysis comparing transcriptomes of pericytes, muLECs, macrophages, larval-stage ECs and embryonic ECs. Full details in Online Methods and **Supplementary Figure 8**. (**c**) Heat-map representation of relative gene expression levels (YuGene analysis; full details in Online Methods) for genes encoding selected markers: known macrophage marker genes *csf1ra*, *stabilin1* and *mafba*; known blood endothelial marker genes *kdrl*, *cdh5*, *sox7*, *sox18* and *tek*; known pericyte marker genes *pdgfrβ* and *notch3*; and known lymphatic endothelial marker genes *lyve1b*, *vegfr3*, *stabilin1*, *stabilin2*, *prox1a*, *nrp2a* and *mafba*. Scale bar indicates relative expression, from 1 (highest) to 0 (lowest). (**d**) Expression levels in reads per kilobase per million mapped reads (RPKM) of endothelial factors in triplicate FAC-sorted muLECs based on RNA-seq data. *Y* axis represents $\log_2(\text{RPKM} + 1)$. Error bars represent mean ± s.e.m. (**e**) Expression levels (RPKM) of neurotrophic factors in triplicate FAC-sorted muLECs based on RNA-seq data. *Y* axis represents $\log_2(\text{RPKM} + 1)$. Error bars represent mean ± s.e.m.

datasets demonstrated that muLECs were a distinct cell type (**Fig. 5b** and **Supplementary Fig. 9e**). Furthermore, when we examined a panel of known cell-type markers, we found that muLECs clustered as a discrete cell type, expressing LEC marker genes (*stabilin1*, *stabilin2*, *mafba*, *flt4* (also called *vegfr3*), *lyve1b*, *nrp2a*, *prox1a*) but not the *csf1r*, pericyte markers *pdgfrβ* or *notch3*, the validated zebrafish microglia marker *apoea*[5] or blood endothelial enriched markers *cdh5* (also called *ve-cadherin*) or *kdrl* (**Fig. 5c**).

We next examined the overall mRNA expression levels of vascular growth factors and secreted regulators of vasculature within the muLEC triplicate RNA-seq dataset. Notably given their mural location, muLECs expressed a range of endothelial growth factors and ligands. Of note, we saw expression from angiogenic growth factors *vegfaa* and *vegfab* and lymphangiogenic factors *vegfc* and *vegfd*, as well as *angpt2a*, *pdgfaa*, *dll4* and *egfl7* (**Fig. 5d**). Despite known roles for ECs in modulating their local environment, the muLECs did not produce neurotrophic factors (**Fig. 5e**). Overall, this extensive expression profiling confirmed the LEC identity of these cells and suggested that they play a role in angiogenesis or vessel maintenance.

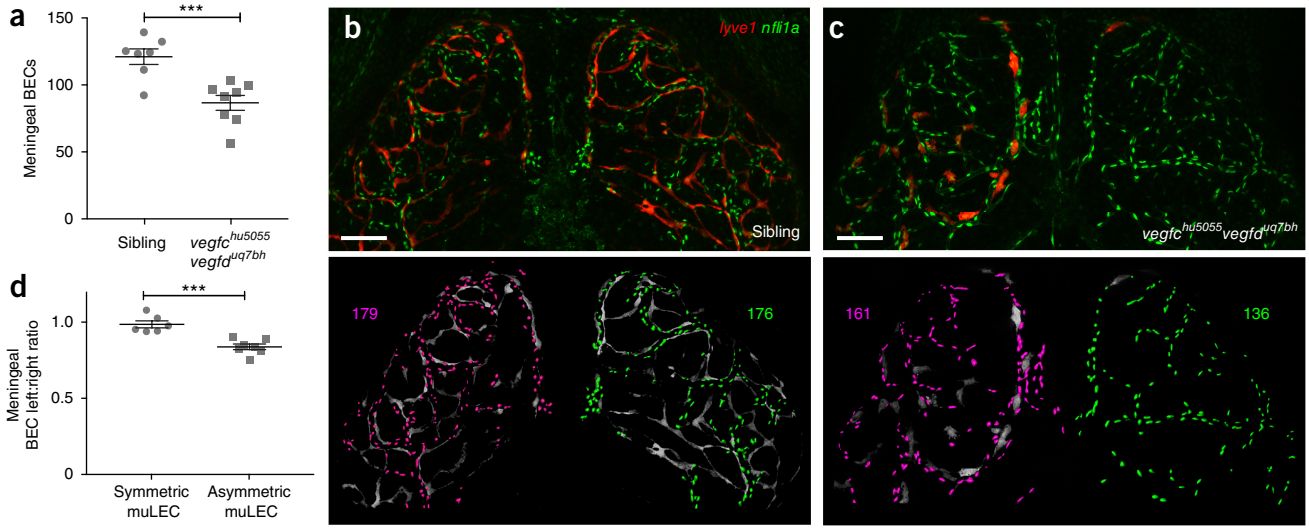

Figure 6 muLECs are correlated with meningeal blood endothelial cell numbers. (**a**) Quantification of meningeal BEC numbers in stage-matched 5.7-mm siblings with normal muLECs and *vegfc*^{hu5055}*vegfd*^{uq7bh} double-mutants lacking muLECs, showing a significant decrease in meningeal BECs. Error bars represent mean ± s.e.m.; ***$P < 0.001$, two-tailed Student's *t* test ($t_{13} = 4.267$; $n = 7$ wild-type vs. 8 mutant larvae). See **Supplementary Figure 10**. (**b**) Top: dorsal confocal image of 6.5-mm *Tg(-5.2lyve1b:DsRed)*^{nz101}*;Tg(fli1a:nEGFP)*^{y7} larvae with symmetrical distribution of muLECs between left and right hemispheres. Bottom: surface render from *z*-stacks showing meningeal BECs and the DsRed signal corresponding to muLECs. The numbers correspond to meningeal BECs on the left and right hemispheres of the brain. Scale bar, 100 µm. (**c**) Top: dorsal confocal image of 6.5-mm *Tg(-5.2lyve1b:DsRed)*^{nz101}*;Tg(fli1a:nEGFP)*^{y7} larvae with asymmetrical distribution of muLECs between left and right hemispheres. Bottom: surface render from a *z*-stack showing meningeal BECs and the DsRed signal corresponding to muLECs. The numbers correspond to meningeal BECs on the left and right hemispheres of the brain. Scale bar, 100 µm. (**d**) Quantification of the ratio of meningeal BECs on the left vs. right hemispheres of the brain in larvae with asymmetrical distributions of muLECs (left/right, where the left side corresponds to the side with more muLECs). There are more BECs on the side of the brain with the most muLECs, leading to a significant loss of BEC symmetry. Error bars represent mean ± s.e.m.; ***$P < 0.001$, two-tailed Student's *t* test ($t_{11} = 5.042$), $n = 6$ symmetric (wild-type) vs. 7 asymmetric (mutant) larvae.

muLECs promote meningeal vascularization

Given that muLECs are closely associated with blood vessels throughout development and produce angiogenic growth factors, we next tested whether they function to promote normal development of the brain vasculature. To determine whether muLECs contribute to blood vessel development, we first analyzed the development of meningeal blood vasculature in zebrafish within a *vegfc*^{hu5055}*vegfd*^{uq7bh} double-mutant background. Specifically, we selected larvae that lacked muLECs and compared the number of meningeal blood endothelial cells (BECs) between mutant and size-matched wild-type sibling larvae. BECs were scored in the region anterior from the junction of the mesencephalic and dorsal longitudinal veins. We found that *vegfc*^{hu5055}*vegfd*^{uq7bh} double mutants, which lack muLECs, had significantly fewer meningeal BECs than stage-matched siblings (**Fig. 6a** and **Supplementary Fig. 10a**,**b**). This difference could be due to the absence of the Vegfc and Vegfd ligands directly controlling blood vessel development, rather than a role of muLECs. Hence, we selected from double-heterozygous incrosses for larvae that had a partial loss of muLECs (given the variable hypomorphic phenotype) and displayed an asymmetric left–right distribution of the remaining muLECs (**Fig. 6b**–**d**). We analyzed the meningeal BEC distribution in these mutant embryos, scoring only the outer BEC nuclei (**Fig. 6c** and **Supplementary Movie 3**). Wild-type embryos were found to have a symmetrical left–right hemisphere distribution of both the muLECs and the meningeal BECs (left–right ratio = 1; **Fig. 6b**,**d**). However, mutants that displayed an asymmetric distribution of muLECs also had an asymmetric distribution of meningeal BECs, with more meningeal BECs on the hemisphere containing more muLECs (**Fig. 6c**,**d**). This observation suggests that the causal factor for this asymmetric meningeal vascularization may be the differential distribution of muLECs.

To directly test whether muLEC function controls local vascularization, we turned to a nongenetic model. We first established that we could measure an increase in meningeal BEC number in the midbrain within a 96-h window beginning at 10 dpf in wild-type larvae (**Fig. 7a**). Next, we directly targeted and ablated muLECs on one side of the brain with a multiphoton laser by visualization in 10-dpf *Tg(-5.2lyve1b:DsRed)*^{nz101}*;Tg(fli1a:nEGFP)*^{s843} larvae (**Fig. 7b**,**c** and **Supplementary Fig. 11a**,**b**). We also performed mock ablations by targeting cells immediately adjacent to the muLECs (**Supplementary Fig. 11c**–**f**) and used these as controls, as well as nonablated control embryos. We quantified meningeal BEC numbers immediately following muLEC ablation and confirmed that we had ablated only the muLECs, without impacting adjacent BECs (**Fig. 7e**,**f**). Ninety-six hours postablation (hpa), we imaged and scored muLECs and meningeal BECs (**Fig. 7d**,**h**,**k**,**l**,**m**). In control and mock-ablated embryos, meningeal BEC numbers increased at similar rates on both sides of the brain and were symmetrically distributed between left and right hemispheres (**Fig. 7g**–**i**,**k**,**m**,**n**). However, muLEC-ablated embryos had reduced meningeal BEC numbers on the ablated side compared with the nonablated side (**Fig. 7j**,**l**,**m**), which resulted in asymmetrical left–right distributions of BECs (**Fig. 7n**). Notably, we observed recovery of muLECs, so that at 96 hpa there was an approximately 50% reduction in muLECs on the ablated side (**Fig. 7o**). We found that the embryos with the greatest recovery of muLECs on the ablated side also had the greatest increase in meningeal BECs on the ablated side (and therefore greater BEC left–right symmetry), as indicated by a positive correlation between meningeal BEC symmetry and muLEC symmetry 96 hpa (**Fig. 7p**). Together, these genetic and cellular ablation data indicate that muLECs, which express an array of endothelial growth factors and ligands, promoted angiogenesis of the developing meningeal blood vasculature.

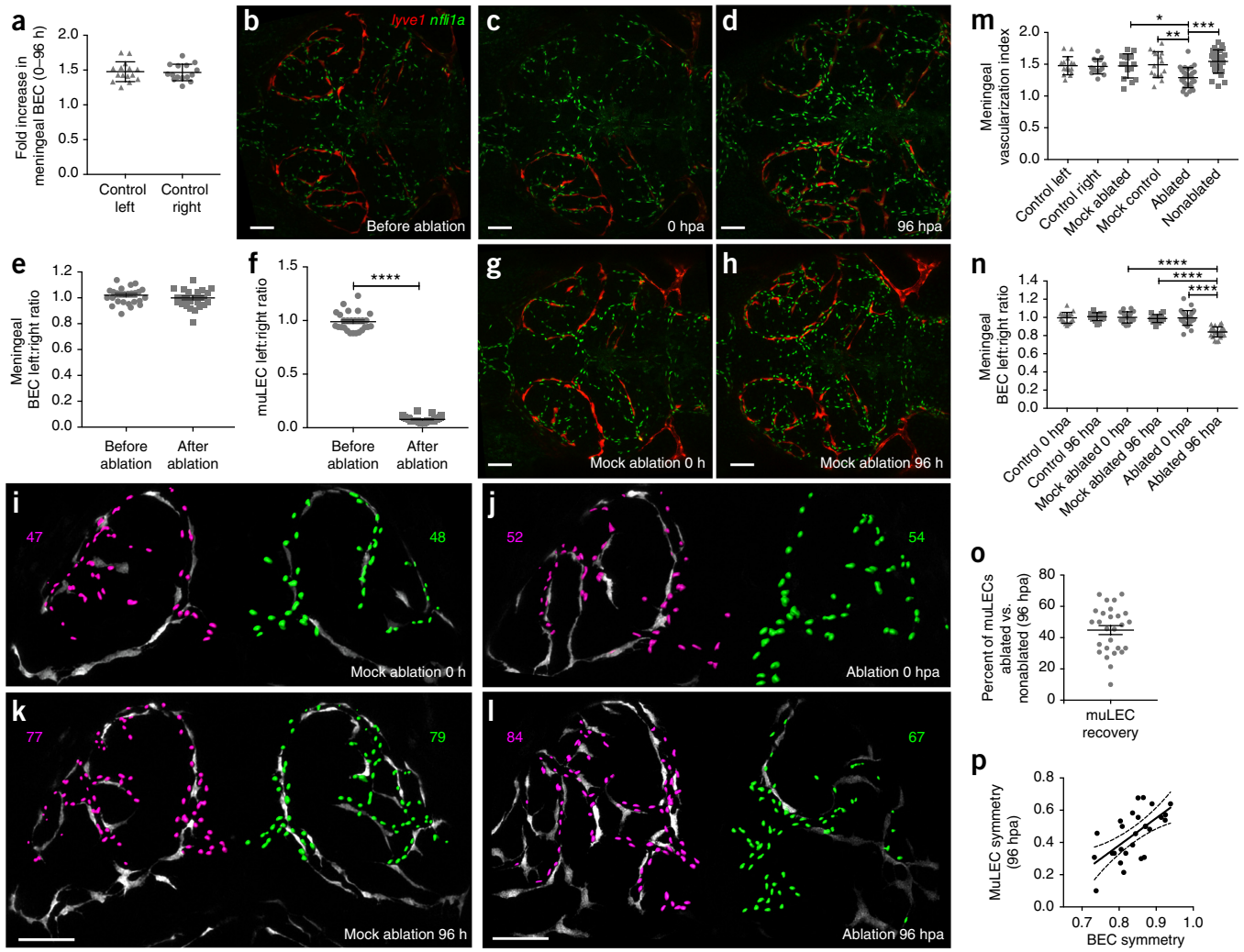

Figure 7 Asymmetric muLEC ablation leads to asymmetric meningeal angiogenesis. (**a**) Quantification of the increase in meningeal BEC number in the 96-h period from 10 dpf in the left and right hemispheres in control (wild-type) brains ($n = 15$ larvae). *Y* axis shows the ratio of cell numbers at 96 h/cell numbers at 0 h. There is no significant difference between the left and right hemispheres ($n = 15$ larvae, $P = 0.8126$, two-tailed Student's *t* test, $t_{28} = 0.2394$). (**b**,**c**) Dorsal confocal images of 10-dpf *Tg(-5.2lyve1b:DsRed)*^{nz101}*;Tg(fli1a:nEGFP)*^{y7} (**b**) before and (**c**) after (0 hpa) multiphoton laser ablation. (**d**) Confocal image of the larvae in **b** and **c** showing BEC (green) and muLEC (red) distribution 96 hpa. (**e**) Quantification of BECs on the left and right hemispheres (*y* axis, ratio of numbers of left/numbers of right BECs) shows there is no change in the left–right symmetry immediately following ablation ($n = 27$ larvae, $P = 0.3024$, two-tailed Student's *t* test, $t_{52} = 1.042$). (**f**) Quantification of muLEC symmetry before and after ablation (*y* axis, ratio of numbers of left/numbers of right BECs). There is a significant difference in muLEC symmetry following ablation (***$P < 0.0001$, two-tailed Student's *t* test, $n = 27$ larvae, $t_{52} = 51.47$). Error bars represent mean ± s.e.m. (**g**,**h**) Dorsal confocal images of 10-dpf control (mock-ablation) embryos (**g**) before and (**h**) 96 hpa (**Supplementary Fig. 11**). Scale bar, 100 µm. (**i**–**l**) Surface render of the *z*-stacks in **b**–**d**, **g** and **h** corresponding to (**i**) 10-dpf and (**k**) 96-hpa mock-ablated and (**j**) 10-dpf and (**l**) 96-hpa muLEC-ablated larvae, respectively, showing rendered meningeal BECs and the DsRed signal (white) corresponding to muLECs. The BECs on the muLEC-ablated and mock-ablated sides are rendered green, and BECs on the nonablated sides are rendered in magenta. Numbers indicate meningeal BECs on the left and right. Ablation experiments were performed to ablate cells adjacent to muLECs (mock ablation, **i**) or the muLECs (**j**). Scale bars, 100 µm. (**m**) Quantification of the vascularization index (number of meningeal BECs at 96 hpa vs. 0 hpa) of BECs on the left and right hemisphere of the brain in control ($n = 15$), mock-ablated ($n = 15$) and muLEC-ablated ($n = 27$) larvae. There was a significant reduction in the expansion in number of meningeal BECs on the muLEC-ablated side of the brain (***$P < 0.001$, **$P < 0.01$, *$P < 0.05$; one-way ANOVA, $F_{5,114} = 6.961$). Error bars represent mean ± s.e.m. (**n**) Quantification of the symmetry of BECs between left and right hemispheres of the brain (*y* axis, left/right BEC number ratio) in control larvae ($n = 15$), mock ablated larvae ($n = 15$) and larvae with muLECs ablated on one side of the brain ($n = 27$ larvae) showing a significant decrease in BEC symmetry 96 hpa. Error bars represent mean ± s.e.m. ****$P < 0.0001$; one-way ANOVA, $F_{5,114} = 28.54$. (**o**) Quantification of the recovery of the muLEC population on the ablated hemisphere expressed as a percentage of the muLECs on the nonablated hemisphere ($n = 27$ larvae). Error bars represent mean ± s.e.m. (**p**) Positive correlation between muLEC symmetry and BEC symmetry 96 hpa (Pearson correlation coefficient, $P = 0.004$; dashed lines represent 95% confidence interval, solid line represents best fit from linear regression, $n = 27$ larvae; $F_{1,25} = 16.63$).

DISCUSSION

The heterogeneity of mural cell types and their biological functions in the vertebrate brain remain to be fully elucidated. The cells of the neurovascular unit are established to play diverse roles in maintaining normal vascular integrity, controlling vascular permeability, serving as a niche for neural stem cells and regulating BBB function[34–36]. Several key regulators of early cerebral angiogenesis have also been described, and major insights have arisen into the molecular control

of new brain vessel formation[37–39]. Nevertheless, we do not currently understand the mechanisms controlling development of many mural cell types or how these cell types interact with each other to modulate the formation and function of the complex patterned neurovasculature. There is also a gap in our understanding of regional differences in mural cells and their interactions in the brain, and the meningeal lineages are yet to be thoroughly scrutinized.

Here while investigating the lymphatic vessels that form around the zebrafish meninx, we identified an unexpected mural LEC population, which we dub muLECs. Notably, this LEC population forms via lymphangiogenesis before transitioning to a mural cell type in an unexpected developmental process (**Supplementary Fig. 12**). Both *vegfc* and *vegfd* are essential for normal muLEC development. Single mutants for either gene displayed reduced lymphangiogenesis, but double mutants displayed a complete or near-complete loss in juvenile and adult stages. Our expression profiling revealed that muLECs express vascular endothelial growth factors and *vegfr3* (*flt4*), which are also crucial for their own development. As such, a degree of autocrine signaling may regulate development and/or maintenance of muLECs, and muLECs may also be prolymphangiogenic in the adult meninx. However, further studies are needed to begin to dissect these potential additional roles.

muLECs produce proangiogenic growth factors known to have roles in angiogenesis and blood vessel maintenance, but they do not produce neurotrophic factors. While multiple cell types are likely to contribute to meningeal vascularization, here we show that muLECs played an important role in this process and were quantitatively responsible for approximately 30% of the expansion of EC numbers immediately following ablation from 10–14 dpf at the meninx (**Fig. 7m**). It also seems likely that they played additional contextual roles, given that these experiments were focused on a narrow developmental window. In adults, muLECs produce Vegfa (aa and ab in zebrafish), as well as an array of vascular growth factors (**Fig. 5**). Notably, Vegfa regulates vascular permeability in mature vessels as well as controlling angiogenesis in new vessels[40–42]. Hence, it is tempting to speculate that muLECs may also play a role in neurovascular homeostasis beyond their role in developmental angiogenesis. Although we did not see any vascular leakage in *vegfc*^{hu5055}*vegfd*^{uq7bh} double-mutant embryos, it is possible that a physiological challenge may be required to reveal additional functions for this cell type.

Together, these data follow the recent characterization of the meningeal lymphatic vascular system that surrounds the brain in mice[9,10] and identify another lineage of the vertebrate brain derived by lymphangiogenesis; in this case, muLECs were derived from blood vessels of the CNS during development. This observation in zebrafish raises the possibility that an equivalent cell type exists in the mammalian brain. The anatomical location of muLECs next to blood vessels, their tendency to locate at branch points, characteristic morphology and expression of several scavenger receptors (for example, Stab1 and Stab2) are highly reminiscent of cell types previously described in the mammalian meninges. It seems likely that muLECs may be the equivalent of previously described lipid-laden cells[30] or fluorescent granular perithelial cells[21,22]. These cell types accumulate lipids and LDL from meningeal blood vessels[22], and we demonstrated that muLECs were capable of performing such functions. It has been suggested that many of these scavenger cell types may be derived from macrophages or monocytes, but evidence of their origin based on lineage-tracing is lacking. We demonstrate that zebrafish muLECs were derived from the endothelium and clearly distinct from macrophages in developmental origin, location and global transcriptomic profile. Further characterization will be needed to determine the equivalent mammalian cell, but with large numbers of Lyve1-expressing cells in mammalian meninges that have not been explored in great detail[9], no formal vascular lineage tracings to the meninges reported and the normally high degree of conservation between zebrafish and mouse development, an equivalent cell type of vascular origin does not seem improbable.

A number of recent studies have suggested significant diversity, organotypic heterogeneity and plasticity in the molecular and cellular mechanisms underpinning lymphangiogenesis[31,43–47]. This study suggests that additional developmental outcomes for LECs have arisen during evolution, perhaps in this case by the specialization of LECs that form in the vertebrate embryonic CNS from local veins in the absence of a selective pressure to form patent functional lymphatics in that tissue. As has been recently noted[48,49], a deeper fundamental understanding of lymphangiogenesis and lymphatic lineages that impact on the CNS is essential and may lead to new opportunities to manipulate CNS homeostasis and pathogenesis in the future.

METHODS

Methods, including statements of data availability and any associated accession codes and references, are available in the online version of the paper.

Note: Any Supplementary Information and Source Data files are available in the online version of the paper.

ACKNOWLEDGMENTS

We thank K. Georgas for design of graphics in the manuscript and thank V. Nink, G. Osborne, H. Chen, D. Paul, J. Springfield and G. Baillie for technical assistance. We thank V. Oorschot and G. Ramm (Ramaciotti Centre for Structural-Cryo Electron Microscopy, Monash Univeristy) for excellent support with electron microscopy. B.M.H. was supported by an NHMRC/NHF Fellowship (1083811); M.F. was supported by an NHMRC Career Development Fellowship (1111169). The Australian Regenerative Medicine Institute is supported by funds from the State Government of Victoria and the Australian Federal Government.

AUTHOR CONTRIBUTIONS

N.I.B. conceived, designed, performed experiments, analyzed data and wrote the manuscript. K.K., C.P.-T., B.W.L., S.P., A.K.L., W.W., S.B., M.R.-G., N.M. and M.F. performed experiments and provided unpublished reagents. I.V., D.G.H., C.A.W., C.S. and S.J.B. performed computational experiments and data analysis. J.K. designed and performed experiments. B.M.H. conceived and designed experiments and wrote the manuscript.

COMPETING FINANCIAL INTERESTS

The authors declare no competing financial interests.

1. Zhao, Z., Nelson, A.R., Betsholtz, C. & Zlokovic, B.V. Establishment and dysfunction of the blood-brain barrier. *Cell* **163**, 1064–1078 (2015).
2. Chakraborty, A., de Wit, N.M., van der Flier, W.M. & de Vries, H.E. The blood brain barrier in Alzheimer's disease. *Vascul. Pharmacol.* **89**, 12–18 (2017).
3. Sweeney, M.D., Ayyadurai, S. & Zlokovic, B.V. Pericytes of the neurovascular unit: key functions and signaling pathways. *Nat. Neurosci.* **19**, 771–783 (2016).
4. Prinz, M., Erny, D. & Hagemeyer, N. Ontogeny and homeostasis of CNS myeloid cells. *Nat. Immunol.* **18**, 385–392 (2017).
5. Abbott, N.J. Astrocyte-endothelial interactions and blood-brain barrier permeability. *J. Anat.* **200**, 629–638 (2002).
6. Aspelund, A., Robciuc, M.R., Karaman, S., Makinen, T. & Alitalo, K. Lymphatic system in cardiovascular medicine. *Circ. Res.* **118**, 515–530 (2016).
7. Li, J., Zhou, J. & Shi, Y. Scanning electron microscopy of human cerebral meningeal stomata. *Ann. Anat.* **178**, 259–261 (1996).
8. Földi, M. *et al.* Lymphogenic haemangiopathy. "Prelymphatic" pathways in the wall of cerebral and cervical blood vessels. *Angiologica* **5**, 250–262 (1968).
9. Louveau, A. *et al.* Structural and functional features of central nervous system lymphatic vessels. *Nature* **523**, 337–341 (2015).
10. Aspelund, A. *et al.* A dural lymphatic vascular system that drains brain interstitial fluid and macromolecules. *J. Exp. Med.* **212**, 991–999 (2015).
11. Carmeliet, P. & Jain, R.K. Molecular mechanisms and clinical applications of angiogenesis. *Nature* **473**, 298–307 (2011).

12. Geudens, I. & Gerhardt, H. Coordinating cell behaviour during blood vessel formation. *Development* **138**, 4569–4583 (2011).
13. Holley, J.E., Newcombe, J., Whatmore, J.L. & Gutowski, N.J. Increased blood vessel density and endothelial cell proliferation in multiple sclerosis cerebral white matter. *Neurosci. Lett.* **470**, 65–70 (2010).
14. Hashimoto, T. *et al.* Evidence of increased endothelial cell turnover in brain arteriovenous malformations. *Neurosurgery* **49**, 124–132 (2001).
15. Arenillas, J.F., Sobrino, T., Castillo, J. & Dávalos, A. The role of angiogenesis in damage and recovery from ischemic stroke. *Curr. Treat. Options Cardiovasc. Med.* **9**, 205–212 (2007).
16. Hogan, B.M. *et al.* Vegfc/Flt4 signalling is suppressed by Dll4 in developing zebrafish intersegmental arteries. *Development* **136**, 4001–4009 (2009).
17. Le Guen, L. *et al.* Ccbe1 regulates Vegfc-mediated induction of Vegfr3 signaling during embryonic lymphangiogenesis. *Development* **141**, 1239–1249 (2014).
18. Villefranc, J.A. *et al.* A truncation allele in vascular endothelial growth factor c reveals distinct modes of signaling during lymphatic and vascular development. *Development* **140**, 1497–1506 (2013).
19. Astin, J.W. *et al.* Vegfd can compensate for loss of Vegfc in zebrafish facial lymphatic sprouting. *Development* **141**, 2680–2690 (2014).
20. Bower, N.I. *et al.* Vegfd modulates both angiogenesis and lymphangiogenesis during zebrafish embryonic development. *Development* **144**, 507–518 (2017).
21. Mato, M. & Ookawara, S. Influences of age and vasopressin on the uptake capacity of fluorescent granular perithelial cells (FGP) of small cerebral vessels of the rat. *Am. J. Anat.* **162**, 45–53 (1981).
22. Mato, M. *et al.* Involvement of specific macrophage-lineage cells surrounding arterioles in barrier and scavenger function in brain cortex. *Proc. Natl. Acad. Sci. USA* **93**, 3269–3274 (1996).
23. Okuda, K.S. *et al.* Lyve1 expression reveals novel lymphatic vessels and new mechanisms for lymphatic vessel development in zebrafish. *Development* **139**, 2381–2391 (2012).
24. Jin, S.-W., Beis, D., Mitchell, T., Chen, J.-N. & Stainier, D.Y.R. Cellular and molecular analyses of vascular tube and lumen formation in zebrafish. *Development* **132**, 5199–5209 (2005).
25. Akitake, C.M., Macurak, M., Halpern, M.E. & Goll, M.G. Transgenerational analysis of transcriptional silencing in zebrafish. *Dev. Biol.* **352**, 191–201 (2011).
26. Ando, K. *et al.* Clarification of mural cell coverage of vascular endothelial cells by live imaging of zebrafish. *Development* **143**, 1328–1339 (2016).
27. Xu, J. *et al.* Temporal-spatial resolution fate mapping reveals distinct origins for embryonic and adult microglia in zebrafish. *Dev. Cell* **34**, 632–641 (2015).
28. Ellett, F., Pase, L., Hayman, J.W., Andrianopoulos, A. & Lieschke, G.J. *mpeg1* promoter transgenes direct macrophage-lineage expression in zebrafish. *Blood* **117**, e49–e56 (2011).
29. Secker, G.A. & Harvey, N.L. VEGFR signaling during lymphatic vascular development: From progenitor cells to functional vessels. *Dev. Dyn.* **244**, 323–331 (2015).
30. Shimabukuro, M.K. *et al.* Lipid-laden cells differentially distributed in the aging brain are functionally active and correspond to distinct phenotypes. *Sci. Rep.* **6**, 23795 (2016).
31. Koltowska, K. *et al.* Mafba is a downstream transcriptional effector of Vegfc signaling essential for embryonic lymphangiogenesis in zebrafish. *Genes Dev.* **29**, 1618–1630 (2015).
32. Liu, C. *et al.* Macrophages mediate the repair of brain vascular rupture through direct physical adhesion and mechanical traction. *Immunity* **44**, 1162–1176 (2016).
33. Lê Cao, K.A., Rohart, F., McHugh, L., Korn, O. & Wells, C.A. YuGene: a simple approach to scale gene expression data derived from different platforms for integrated analyses. *Genomics* **103**, 239–251 (2014).
34. Lojewski, X. *et al.* Perivascular mesenchymal stem cells from the adult human brain harbor no instrinsic neuroectodermal but high mesodermal differentiation potential. *Stem Cells Transl. Med.* **4**, 1223–1233 (2015).
35. Armulik, A. *et al.* Pericytes regulate the blood-brain barrier. *Nature* **468**, 557–561 (2010).
36. Zonta, M. *et al.* Neuron-to-astrocyte signaling is central to the dynamic control of brain microcirculation. *Nat. Neurosci.* **6**, 43–50 (2003).
37. Siekmann, A.F., Standley, C., Fogarty, K.E., Wolfe, S.A. & Lawson, N.D. Chemokine signaling guides regional patterning of the first embryonic artery. *Genes Dev.* **23**, 2272–2277 (2009).
38. Covassin, L.D., Villefranc, J.A., Kacergis, M.C., Weinstein, B.M. & Lawson, N.D. Distinct genetic interactions between multiple Vegf receptors are required for development of different blood vessel types in zebrafish. *Proc. Natl. Acad. Sci. USA* **103**, 6554–6559 (2006).
39. Vanhollebeke, B. *et al.* Tip cell-specific requirement for an atypical Gpr124- and Reck-dependent Wnt/β-catenin pathway during brain angiogenesis. *Elife* http://dx.doi.org/10.7554/eLife.06489 (2015).
40. Keck, P.J. *et al.* Vascular permeability factor, an endothelial cell mitogen related to PDGF. *Science* **246**, 1309–1312 (1989).
41. Carmeliet, P. *et al.* Abnormal blood vessel development and lethality in embryos lacking a single *VEGF* allele. *Nature* **380**, 435–439 (1996).
42. Bahary, N. *et al.* Duplicate *vegfa* genes and orthologues of the KDR receptor tyrosine kinase family mediate vascular development in the zebrafish. *Blood* **110**, 3627–3636 (2007).
43. Klotz, L. *et al.* Cardiac lymphatics are heterogeneous in origin and respond to injury. *Nature* **522**, 62–67 (2015).
44. Wigle, J.T. & Oliver, G. Prox1 function is required for the development of the murine lymphatic system. *Cell* **98**, 769–778 (1999).
45. Stanczuk, L. *et al.* cKit lineage hemogenic endothelium-derived cells contribute to esenteric lymphatic vessels. *Cell Rep.* http://dx.doi.org/10.1016/j.celrep.2015.02.026 (2015).
46. Martinez-Corral, I. *et al.* Nonvenous origin of dermal lymphatic vasculature. *Circ. Res.* https://doi.org/10.1161/CIRCRESAHA.116.306170 (2015).
47. Nicenboim, J. *et al.* Lymphatic vessels arise from specialized angioblasts within a venous niche. *Nature* **522**, 56–61 (2015).
48. Dissing-Olesen, L., Hong, S. & Stevens, B. New brain lymphatic vessels drain old concepts. *EBioMedicine* **2**, 776–777 (2015).
49. Bakker, E.N. *et al.* Lymphatic clearance of the brain: perivascular, paravascular and significance for neurodegenerative diseases. *Cell. Mol. Neurobiol.* **36**, 181–194 (2016).

ONLINE METHODS

Zebrafish. All zebrafish strains were maintained at the University of Queensland under standard husbandry conditions with a 14-h light 10-h dark cycle. Animal experiments were performed in accordance with the guidelines of the animal ethics committee at the University of Queensland. The previously published transgenic lines used were *Tg(fli1a:nEGFP)^{y7}* (ref. 50, *Tg(fli1a: EGFP)^{y1}* (ref. 51), *TgBAC(prox1a:KaltA4)^{uq3bh}* (ref. 52), *Tg(kdrl:EGFP)^{s843}* (ref. 24) and *Tg(kdrl:mcherry)^{s843}*, *TG(flt1:YFP)^{hu4624}* (ref. 53) and *Tg(-5.2lyve1b:DsRed)^{nz101}* (ref. 23). The *TgBAC(prox1a:KalTA4-4xUAS-ADV.E1b:TagRFP)^{nim5}* (refs. 54,55), *Tg(mpeg1:mcherry)* (ref. 28), *Tg(nkx2.2a:EGFP)^{vu16Tg}* (ref. 56) and *Tg(10xUAS: Kaede)^{s1999t}* (ref. 57). The *vegfc^{hu5055}* allele and *vegfr3*/*flt4^{hu4062}* allele have been previously described[17,53].

Transgenic line generation for this study. The *TgBAC(pdgfrβ:EGFP)^{uq15bh}* construct was produced previously[26] and used to generate an independent transgenic line. The *TgBAC(acta2:EGFP)^{uq17bh}* construct was generated as previously described[53] by recombineering of the BAC clone DKEY-256C3. The transgenic lines, including *Tg(-5.2lyve1b:BFPCaax)^{uq18bh}* and *Tg(-5.2lyve1b:Venus)^{uq16bh}* were generated by Tol2-mediated transgenesis, as previously described[31]. *Tg(-5.2lyve1b:BFPCaax)^{uq18bh}* and *Tg(-5.2lyve1b:Venus)^{uq16bh}* were generated using Gateway cloning[58]. To generate the transgenic strains, 20 ng/μL of plasmid DNA and 25 ng/μL of *tol2* transposase mRNA were injected in one-cell-stage embryos, and F1 founders were identified by the presence of EGFP expression in the eye, driven by the α-crystallin promoter.

Morpholino injections. The *flt4* and *ccbe1* morpholinos have been previously described[53].

Genotyping. DNA extraction from fin clips and embryos was performed as previously described[59]. Genotyping for *vegfd^{uq7bh}* and *vegfc^{hu5055}* mutants was performed using KASP assays (LGC Genomics) on an ABI Via7 qPCR machine with the following primer sequences:

vegfd wild-type allele: GGATGAGCTTCTGATGTTGACCG;
vegfd mutant allele: GGATGAGCTTCTGATGTTGACCC;
vegfd common primer: GCTTGAGTCTGCATCTCCACAACTT;
vegfc wild-type allele: CAGCTGTGTCCGGCCTCCAT;
vegfc mutant allele: AGCTGTGTCCGGCCTCCAC; and
vegfc common primer: TTTCCTTCTCTTGGGGTCCACGTTA.

FAC sorting, RNA amplification and RNA-seq. FAC sorting was performed as previously described[60]. Cells from 8 male and female 12-month-old *Tg(-5.2lyve1b:DsRed)^{nz101}* adult zebrafish brains (without lymphatic vessels) were collected into Trizol LS reagent (Life Technologies) and extracted using a DirectZol RNA extraction kit (Zymo research). For pericyte isolation, cells from 4 male and female 3-month-old *TgBAC(pdgfrβ:EGFP)^{uq15bh}* adult zebrafish brains were FAC-sorted as above. RNA integrity was determined using a Bioanalyser (Agilent) and RNA amplification performed as previously described[61]. RNA-seq was performed on three separate biological replicates using a Nextera XT library kit and Next seq sequencer (Illumina) at the IMB sequencing facility.

RNA-seq data analysis and comparison of muLEC and selected transcriptomes. Illumina sequence reads were mapped against Illumina's zv9 iGenomes assembly using STAR 2.4.2a[62], and gene-level read counts were generated using htseq-count[63] with the gene_name id attribute.

For **Figure 5a**, a set of three control zebrafish RNA-seq samples were chosen to encompass variation in postembryonic zebrafish tissues; adult head (GEO: GSM977959), adult tail (GEO: GSM977960) and 5-day larva (GEO: GSM977958). Differential expression was assessed between FAC-sorted cells and the control sample set using DESeq2 (ref. 64). All available Ensembl gene identifiers for human orthologs were identified using Ensembl BioMart. Human Ensembl IDs for all genes called by DESeq as upregulated in FAC-sorted cells with an adjusted $P < 0.001$ were analyzed with the HOMER v4.7 software package[65], and results for all Gene Ontology (GO) terms in the Biological Process hierarchy were retained. GO terms were filtered using GOtrim v2.0[66], with a soft-trimming threshold of 0.2 (parent term is trimmed if it has < 20% genes not in child term), and terms with three or fewer target genes were excluded. Bonferroni-adjusted *P* values for all GO terms retained after this procedure were evaluated using R with a significance threshold of $P < 0.05$. Using these parameters, 520 zebrafish genes were called as differentially expressed at an adjusted *P* value threshold of $P < 0.001$, of which 395 had an ortholog mapping in the human genome. Of 12,871 Biological Process GO term IDs, 1,105 had more than three target genes, and of those, 356 were trimmed by GOtrim, leaving 749 terms in the analysis.

Data processing. SRR files retrieved from the sequence read archive (SRA) were converted to FASTQ using the fastq-dump utility from the sra-tools package v2.4.3 (http://ncbi.github.io/sra-tools/). FASTQ were aligned to the GRCz10 build of the *Danio rerio* genome and summarized at a metafeature (gene) level according to the Ensembl version 86 annotation. Alignment and summarization of reads was performed with RSubread v1.20.6 (https://bioconductor.org/packages/release/bioc/html/Rsubread.html)[67]. Counts were converted to $\log_2$ counts per million (with a hard floor of +1 count to prevent negative log values). These values were then scaled using the cumulative proportion with the YuGene transformation to normalize for batch[33]. Processing was done using pandas v0.19.2 (http://pandas.pydata.org)[68] in Python v3.6.0 (https://www.python.org).

Dataset sources. We used existing RNA-seq data that was publicly available from transgenic brain-derived endothelial cells from *Tg(flk1:DenNTR)* larvae (SRA ID: SRP070686)[32]; transgenic brain-derived macrophages from *Tg(coro1a: Kaeda; flk1:EGFP)* larvae (SRA ID: SRP070686)[32]; our previously published 2-dpf endothelial cell analyses (GEO ID pending as of April 2017)[31]; adult pericytes isolated from the brain from this study (GEO ID pending); and adult mural LECs isolated from this study (GEO ID pending).

Data clustering and analysis. Principal component analysis was performed on the YuGene transformed values using scikit-learn v0.18.1 (http://scikit-learn.org)[69] and plotted using matplotlib v2.0.0 (http://matplotlib.org; doi:10.5281/zenodo.248351).

Heat maps of selected genes, clustered by Euclidean distance on their YuGene values, were created using the clustermap function from the seaborn package v0.7.1 (http://seaborn.pydata.org; doi:10.5281/zenodo.54844).

Photoconversion of Kaede-expressing cells. For photoconversion of Kaede-expressing cells, *Tg(prox1a:KaltA4)^{uq3bh};Tg(10xUAS:Kaede)^{s1999t}* embryos and larvae were mounted in low-melting-point agarose. Initial imaging was performed using laser and filter settings optimized for EGFP and rhodamine. Images were acquired and then cells photoconverted using a Zeiss LSM 710 FCS confocal microscope by exposing the target cells via a *z*-stack to a 405-nm laser set at 4.0% power for 5 min. Consistent with the reported stability of Kaede photoconversion[70], we were able to detect converted protein for several days of development. Following photoconversion, cells were reimaged using the same settings as used for the image obtained before photoconversion. To trace the photoconverted cells, the same region was reimaged 5 d after photoconversion, using the same settings.

Lymphangiography and angiography. To assess the ability of muLECs and meningeal lymphatics to take up dye, 2,000 kDa high-molecular-weight FITC-labeled dextran (Invitrogen) was injected into the dorsal midbrain region of 7-mm larvae anesthetized with MS-222 using capillary glass needles. The same dye was injected into the posterior cardinal vein to assess vascular leakage in 7-mm mutant and wild-type larvae. Angiography was performed by injecting 10 kDa dextran blue dye (Invitrogen) into the atrium of 5-dpf zebrafish embryos.

Immunoelectron microscopy labeling of muLECs. Adult brains from the *Tg(-5.2lyve1b:Venus)* line ($n = 2$) were excised and the telencephalon isolated for fixation and embedding as described[71]. Briefly, telencephalons were fixed in a mixture of 2% paraformaldehyde, 0.2% glutaraldehyde and 4% sucrose in 0.1 M phosphate buffer (PB) at 4 °C overnight and washed the following day with 0.15% glycine diluted in 1× phosphate buffered saline (pH 7.4). Telencephalons were infused in 6% gelatin in PB at 37 °C for 60 min before being solidified on ice and postfixed in 0.5% paraformaldehyde in 0.1 M PB for 30 min at 4 °C. Thereafter, gelatin blocks were briefly rinsed with ice cold buffer and infiltrated in 2.3 M sucrose for 2 d at 4 °C on the rocker. In preparation for sectioning, sucrose infiltrated gelatin-tissue blocks were mounted on an aluminum pin and frozen in liquid nitrogen. We cut 80-nm ultrathin sections on a Leica UC7/FC7 Ultramicrotome at −100 °C using a Diatome diamond knife and collected them on carbon-coated 50-mesh copper grids containing formvar film.

Immunolabeling was performed as previously described[72] using goat anti-GFP-biotin (Rockland, 600-106-215), rabbit anti-biotin (Rockland, 100-4198) and Protein A gold 15-nm (Dept. of Cell Biology, UMC Utrecht, Netherlands). Following immunolabeling, sections were stained in uranyl oxalate and methylcellulose/uranyl acetate. Grids were looped out and air-dried before imaging on a Hitachi H7500 TEM at 80 kV with a Gatan multiscan camera (1 K × 1 K). The position of muLECs in relation to endothelial cells was imaged at the highly vascularized lateral junction between the dorsal and ventral telencephalon where the large blood vessel enters.

Ablation experiments. Zebrafish *Tg(-5.2lyve1b:DsRed)*^{nz101}*;Tg(fli1a:nEGFP)*^{y7} larvae were grown in PTU and at 10 dpf were ventrally mounted in 0.5% low-melting-point agarose. DsRed-positive muLECs and EGFP-positive BECs were identified using 561-nm and 488-nm lasers, respectively, and DsRed-positive cells ablated using a two-photon laser at 790 nm (Mai Tai, Spectr-Physics Millenia PRO). Control ablations were performed as above, with a cell adjacent to the muLEC targeted; successful ablation was confirmed through collection of transmitted light (for examples see **Supplementary Fig. 11**). Larvae were imaged before and after ablation using the same settings and then again at 96 hpa. In larvae that displayed successful ablation, meningeal BECs were quantified manually using ImageJ or Imaris software.

Imaging. Imaging was performed in the Australian Cancer Research Foundation's Dynamic Imaging Facility at the Institute for Molecular Bioscience. Live zebrafish embryos were mounted laterally or ventrally in 0.5% low-melting-point agarose and imaged using a Zeiss LSM 710 FCS confocal microscope. Images were processed using ImageJ 1.47 software (National Institute of Health) or the Imaris suite.

Data collection. Larvae were collected from incrosses of several pairs of adult zebrafish. Mutant and sibling larvae were grown together in a single tank. Phenotyping preceded genotyping in mutant analyses, hence analysis was genotype blinded. For ablation experiments, larvae were randomly selected from the same tank at 10 dpf. For ablation experiments, data collection and analysis were not performed blind due to the conditions of the experiments. Larval staged animals were used before sexual maturity, and there were no sex-specific differences in muLECs observed in adults.

Statistical analysis. Statistical analysis (*t* tests and ANOVA) were performed using Prism software (GraphPad). Data were tested to meet parametric assumptions (D'Agostino–Pearson test for normality, Brown-Forsythe test for variance), and then ANOVA with Fisher's individual-error *post hoc* test was used to identify significant differences. Student's *t* test was used for comparison of two means. No statistical methods were used to predetermine sample sizes, but our sample sizes are similar to those reported previously[23,50].

A **Supplementary Methods Checklist** is available.

Data availability. RNA-seq data will be made publicly available at GEO accession codes GSE97649, GSE97650 and GSE97651. The data that support the findings of this study are available from the corresponding author upon reasonable request.

50. Roman, B.L. *et al.* Disruption of *acvrl1* increases endothelial cell number in zebrafish cranial vessels. *Development* **129**, 3009–3019 (2002).
51. Lawson, N.D. & Weinstein, B.M. *In vivo* imaging of embryonic vascular development using transgenic zebrafish. *Dev. Biol.* **248**, 307–318 (2002).
52. Koltowska, K. *et al.* Vegfc regulates bipotential precursor division and Prox1 expression to promote lymphatic identity in zebrafish. *Cell Rep.* **13**, 1828–1841 (2015).
53. Hogan, B.M. *et al.* Ccbe1 is required for embryonic lymphangiogenesis and venous sprouting. *Nat. Genet.* **41**, 396–398 (2009).
54. Dunworth, W.P. *et al.* Bone morphogenetic protein 2 signaling negatively modulates lymphatic development in vertebrate embryos. *Circ. Res.* **114**, 56–66 (2014).
55. van Impel, A. *et al.* Divergence of zebrafish and mouse lymphatic cell fate specification pathways. *Development* **141**, 1228–1238 (2014).
56. Ng, A.N. *et al.* Formation of the digestive system in zebrafish: III. Intestinal epithelium morphogenesis. *Dev. Biol.* **286**, 114–135 (2005).
57. Scott, E.K. *et al.* Targeting neural circuitry in zebrafish using GAL4 enhancer trapping. *Nat. Methods* **4**, 323–326 (2007).
58. Hartley, J.L., Temple, G.F. & Brasch, M.A. DNA cloning using *in vitro* site-specific recombination. *Genome Res.* **10**, 1788–1795 (2000).
59. Dahlem, T.J. *et al.* Simple methods for generating and detecting locus-specific mutations induced with TALENs in the zebrafish genome. *PLoS Genet.* **8**, e1002861 (2012).
60. Coxam, B. *et al.* Pkd1 regulates lymphatic vascular morphogenesis during development. *Cell Rep.* **7**, 623–633 (2014).
61. Picelli, S. *et al.* Full-length RNA-seq from single cells using Smart-seq2. *Nat. Protoc.* **9**, 171–181 (2014).
62. Dobin, A. *et al.* STAR: ultrafast universal RNA-seq aligner. *Bioinformatics* **29**, 15–21 (2013).
63. Anders, S., Pyl, P.T. & Huber, W. HTSeq – A Python framework to work with high-throughput sequencing data. *Bioinformatics* **31**, 166–169 (2015).
64. Love, M.I., Huber, W. & Anders, S. Moderated estimation of fold change and dispersion for RNA-seq data with DESeq2. *Genome Biol.* **15**, 550 (2014).
65. Heinz, S. *et al.* Simple combinations of lineage-determining transcription factors prime *cis*-regulatory elements required for macrophage and B cell identities. *Mol. Cell* **38**, 576–589 (2010).
66. Jantzen, S.G., Sutherland, B.J., Minkley, D.R. & Koop, B.F.G.O. GO Trimming: systematically reducing redundancy in large Gene Ontology datasets. *BMC Res. Notes* **4**, 267 (2011).
67. Liao, Y., Smyth, G.K. & Shi, W. The Subread aligner: fast, accurate and scalable read mapping by seed-and-vote. *Nucleic Acids Res.* **41**, e108 (2013).
68. McKinney, W. Data structures for statistical computing in Python. *Proc. 9th Python Sci. Conf.* 51–56 (2010).
69. Pedregosa, F. *et al.* Scikit-learn: machine learning in Python. *J. Mach. Learn. Res.* **12**, 2825–2830 (2011).
70. Hatta, K., Tsujii, H. & Omura, T. Cell tracking using a photoconvertible fluorescent protein. *Nat. Protoc.* **1**, 960–967 (2006).
71. Oorschot, V.M., Sztal, T.E., Bryson-Richardson, R.J. & Ramm, G. Immuno correlative light and electron microscopy on Tokuyasu cryosections. *Methods Cell Biol.* **124**, 241–258 (2014).
72. Slot, J.W. & Geuze, H.J. Cryosectioning and immunolabeling. *Nat. Protoc.* **2**, 2480–2491 (2007).